The Astrophysical Journal, 881:71 (14pp), 2019 August 10 https://doi.org/10.3847/1538-4357/ab211a
© 2019. The American Astronomical Society. All rights reserved.

A Closer Look at Bursty Star Formation with $L_{\mathrm{H}\alpha}$ and L_{UV} Distributions

Najmeh Emami[1], Brian Siana[1], Daniel R. Weisz[2], Benjamin D. Johnson[3], Xiangcheng Ma[2], and Kareem El-Badry[2]
[1] Department of Physics and Astronomy, University of California Riverside, Riverside, CA 92521, USA
[2] Department of Astronomy, University of California Berkeley, Berkeley, CA 94720, USA
[3] Harvard-Smithsonian Center for Astrophysics, Cambridge, MA 02138, USA
Received 2018 September 15; revised 2019 May 9; accepted 2019 May 10; published 2019 August 13

Abstract

We investigate the bursty star formation histories (SFHs) of dwarf galaxies using the distribution of $\log(L_{\mathrm{H}\alpha}/L_{\mathrm{UV}})$ of 185 local galaxies. We expand on the work of Weisz et al. to consider a wider range of SFHs and stellar metallicities, and show that there are large degeneracies in a periodic, top-hat burst model. We argue that all galaxies of a given mass have similar SFHs and we can therefore include the $L_{\mathrm{H}\alpha}$ distributions (subtracting the median trend with stellar mass, referred to as $\Delta\log(L_{\mathrm{H}\alpha})$) in our analyses. $\Delta\log(L_{\mathrm{H}\alpha})$ traces the amplitude of the bursts, and $\log(L_{\mathrm{H}\alpha}/L_{\mathrm{UV}})$ is a function of the timescale, amplitude, and shape of the bursts. We examine the two-dimensional distribution of these two indicators to constrain the SFHs. We use exponentially rising/falling bursts to determine timescales (*e*-folding time, τ). We find that galaxies below $10^{7.5}$ $M_{\odot}$ undergo large (maximum amplitudes of $\sim$100) and rapid ($\tau < 30$ Myr) bursts, while galaxies above $10^{8.5}$ $M_{\odot}$ experience smaller (maximum amplitudes $\sim$10), slower ($\tau \gtrsim 300$ Myr) bursts. We compare with the FIRE-2 hydrodynamical simulations and find that the burst amplitudes agree with observations, but they are too rapid in intermediate-mass galaxies ($M_{*} > 10^{8}$ $M_{\odot}$). Finally, we confirm that stochastic sampling of the stellar mass function cannot reproduce the observed distributions unless the standard assumptions of cluster and stellar mass functions are changed. With the next generation of telescopes, measurements of L_{UV} and $L_{\mathrm{H}\alpha}$ will become available for dwarf galaxies at high redshift, enabling similar analyses of galaxies in the early universe.

Key words: galaxies: dwarf – galaxies: evolution – galaxies: formation – galaxies: star formation

1. Introduction

An active area of research in galaxy evolution is understanding "feedback"—energy and/or momentum deposition into the interstellar medium—from stars and accreting black holes. It is generally believed that star formation is suppressed in high-mass galaxies by feedback from the central, supermassive black holes and in dwarf galaxies by feedback from massive stars (photoionization heating, stellar winds, radiation pressure, and supernovae) (Somerville & Primack 1999; Springel et al. 2005; Kereš et al. 2009; Governato et al. 2010; Hopkins et al. 2014).

However, there are still significant uncertainties in how the various forms of feedback couple with the gas and the efficiency with which it heats or expels gas. The implementation of different sub-grid prescriptions for stellar feedback in hydrodynamical simulations can result in markedly different predictions of the characteristics of galaxies. One generic feature of hydrodynamical simulations of dwarf galaxies that include strong stellar feedback is large variations in the star formation rates (SFRs), often referred to as "bursty" star formation. Simulations with different feedback prescriptions produce bursts of star formation with very different characteristics (e.g., amplitude and duration). Because it is in principle possible to observe large variations in SFR, observers can test these feedback prescriptions to better understand the physical mechanisms that regulate star formation in dwarf galaxies.

The primary method by which one can measure the burstiness is to use indicators (observables) of star formation that trace different timescales. The two most common indicators are the luminosity of the (non-scattering) hydrogen recombination lines (such as Hα and Hβ) and the far-ultraviolet (far-UV) continuum (1300 Å $< \lambda <$ 2000 Å) luminosity density (L_{UV}). Hereafter we refer to the logarithm of the ratio of these two observables, $\log(L_{\mathrm{H}\alpha}/L_{\mathrm{UV}})$. $L_{\mathrm{H}\alpha}$ is a byproduct of the ionizing radiation from short-lived O-stars. Therefore, during an episode of constant star formation, $L_{\mathrm{H}\alpha}$ equilibrates rapidly, as the rate of O-star supernovae equals the rate of O-star formation. L_{UV}, on the other hand, is produced by O-stars as well as longer-lived B-stars and A-stars. Therefore, L_{UV} takes much longer to reach equilibrium after an episode of constant star formation. Using the stellar population synthesis models of Bruzual & Charlot (2003) for constant star formation, we find equilibrium timescales (reaching 90% of the equilibrium value, Kennicutt & Evans 2012) of 5 and 100 Myr for $L_{\mathrm{H}\alpha}$ and L_{UV}, respectively. Because of this, both $L_{\mathrm{H}\alpha}$ and L_{UV} accurately trace the SFR of any galaxy whose SFR changes on timescales much longer than 100 Myr. Thus, the ratio, $\log(L_{\mathrm{H}\alpha}/L_{\mathrm{UV}})$, remains approximately constant. However, if the SFR changes on shorter timescales than 100 Myr, L_{UV} will no longer follow the SFR and the ratio, $\log(L_{\mathrm{H}\alpha}/L_{\mathrm{UV}})$, will vary. Therefore, the distribution of $\log(L_{\mathrm{H}\alpha}/L_{\mathrm{UV}})$ can inform whether or not the SFR of galaxies changes on timescales less than 100 Myr.

We note that these observables ($L_{\mathrm{H}\alpha}$, L_{UV}) are often used to determine physical properties of galaxies such as SFR and the efficiency of ionizing photon production (ξ_{ion}) (Robertson et al. 2013; Bouwens et al. 2015; Duncan & Conselice 2015) under the assumption that star formation varies slowly with time. Therefore, understanding bursty star formation is critical for interpreting these observables (Domínguez et al. 2015).

There have been several analyses of the distributions of $L_{\mathrm{H}\alpha}/L_{\mathrm{UV}}$ attempting to extract information about the typical amplitudes, durations, and periods of the bursts (Glazebrook et al. 1999; Iglesias-Páramo et al. 2004; Lee et al. 2011; Weisz et al. 2012; Kauffmann 2014; Domínguez et al. 2015). Several factors other than star formation history (SFH) can affect

$L_{H\alpha}/L_{UV}$, as discussed by Iglesias-Páramo et al. (2004), Boselli et al. (2009), Lee et al. (2009), Meurer et al. (2009), and Guo et al. (2016). Here, we list all of these factors other than the SFH (which is the subject of this paper) and briefly explain how they affect $L_{H\alpha}/L_{UV}$.

1. Dust extinction. Because dust extinction is often a strong function of wavelength, and the nebular and stellar UV continuum emission can arise from stars with different spatial distributions relative to dust, the effect of dust on the observed $L_{H\alpha}/L_{UV}$ can be considerable (Kewley et al. 2002; Lee et al. 2009).
2. Escape of ionizing photons. If ionizing photons are escaping from the galaxy (Steidel et al. 2001; Shapley et al. 2006; Siana et al. 2007), the photoionization rate (and therefore $L_{H\alpha}$) will be lower than expected under the assumption that all ionizing photons are absorbed in H II regions.
3. Initial stellar mass function (ISMF). $L_{H\alpha}/L_{UV}$ is influenced by the relative number of stars at each mass, so variations in the ISMF will affect the ratio. This can include "effective ISMFs," where the star-forming clouds are not sufficiently massive to fully sample the high-mass end of the ISMF (Pflamm-Altenburg et al. 2007, 2009; Hoversten & Glazebrook 2008). The initial cluster mass function can also affect these "effective ISMFs" because it determines the relative numbers of clusters that do and do not fully sample the high-mass end of the ISMF.
4. Stellar metallicity. Stars with lower metal abundances will be hotter at the same mass, resulting in higher $L_{H\alpha}/L_{UV}$(Bicker & Fritze-v. Alvensleben 2005; Boselli et al. 2009).
5. Stellar models. Inclusion of binaries (Eldridge 2012) and rotating stars (Choi et al. 2017) in the stellar evolution modeling will increase $L_{H\alpha}/L_{UV}$.

There are several papers discussing these effects on the $L_{H\alpha}/L_{UV}$ distribution, but many have concluded that the most important effects are bursty star formation and (or) variations in the initial mass function (IMF) (Meurer et al. 2009; Guo et al. 2016; Mehta et al. 2017). The main focus of this paper is to use observable distributions to better understand bursty star formation. Specifically, we aim to: (1) more fully explore the parameter space of bursty star formation models; (2) break degeneracies and minimize uncertainties in these models; (3) determine typical timescales for the rise/fall of star formation as a function of galaxy stellar mass; (4) better understand whether burstiness or IMF variations explain the observed $L_{H\alpha}/L_{UV}$ distributions.

First we describe the observational data that will be used throughout this paper in Section 2. In Section 3, we review previous efforts to determine the burstiness parameters (amplitude, period, duration) using the $L_{H\alpha}/L_{UV}$ distribution. We also introduce our improved method to more completely explore the parameter space and compare with previous results. In Section 4.1, we propose combining the $L_{H\alpha}$ distribution with the $L_{H\alpha}/L_{UV}$ distribution to better constrain bursty star formation models. In Section 4.2, we introduce a new exponential burst model to better constrain the timescales for the rise and fall of SFRs in dwarf galaxies. In Section 5, we compare with predictions from hydrodynamical simulations and discuss the physical implications. We also examine the effect of stochastic IMF sampling on our analysis and discuss the results in this section as well as the effects of escape fraction and dust attenuation on the observed distribution.

2. Observational Data

In this work, we use the same far-UV and Hα photometry as Weisz et al. (2012, hereafter W12) from the 11 Mpc Hα and UV Galaxy Survey (11HUGS, Kennicutt et al. 2008; Lee et al. 2009). The primary sample is complete in including all nearby galaxies within 11 Mpc and consists of spirals and irregulars that avoid the Galactic plane ($|b| > 20^{\circ}$) and are brighter than $B = 15$ mag. Stellar masses were determined using optical photometry from the Sloan Digital Sky Survey and *Spitzer* mid-IR (IRAC) photometry from the Local Volume Legacy Survey. Thus the W12 sample is a subsample of 11HUGS galaxies for which their optical and IR measurements are available. The data are corrected for both Galactic foreground dust extinction and extinction within the target galaxy. See W12 and Lee et al. (2009) for further details and sample completeness. We decided to remove five galaxies with either $\log(L_{H\alpha}/L_{UV}) < -3.4$ or $\log(L_{H\alpha}/L_{UV}) > -1.8$ from the sample. Two of the outliers (UGCA 281, MRK 475) are Wolf–Rayet galaxies. The other three outliers have extremely high or low $\log(L_{H\alpha}/L_{UV})$ such that the stellar synthesis models are not able to reproduce them (UGCA 438, KDG 61, UGC 7408).

3. Review of the Methods

Below, we discuss the methods used in previous studies and argue the strengths and shortcomings of those methods.

Iglesias-Páramo et al. (2004) and Boselli et al. (2009) considered instantaneous bursts of SF superimposed on a baseline with a few different time intervals between bursts. Meurer et al. (2009) used an SF model of Gaussian bursts added to (or "gasps" subtracted from) a constant SFR, in which the FWHM of the Gaussians represents the duration and also affects timescale for fractional changes in SFR. All three studies assumed discrete model parameters and did not fully and systematically explore the parameter space. It is noteworthy that Boselli et al. (2009) were the first to introduce different model parameters for galaxies of different stellar masses, pointing out that low-mass galaxies show a larger spread in the $\log(L_{H\alpha}/L_{UV})$ distribution. They conclude that this larger spread in the $\log(L_{H\alpha}/L_{UV})$ distribution is due to sporadic bursts of SF (with periods of 10 Myr), whereas the small spread in the $\log(L_{H\alpha}/L_{UV})$ distribution of massive galaxies suggests a roughly constant SFR.

W12 made a notable step forward and divided their observed sample into five stellar mass bins from 10^6 to 10^{11} $M_{\odot}$ and assumed that all galaxies of similar stellar masses have SFHs with the same parameters and could be considered random samples in time of each SFH. They defined their SF models as top-hat, periodic bursts superimposed on a constant baseline. They then determined the $\log(L_{H\alpha}/L_{UV})$ distribution from models with different burst periods (P, the time interval between two consecutive bursts), durations (D, the time during which the star formation is in burst), and amplitudes (A, the SFR at burst relative to the baseline SFR) and used a Kolmogorov–Smirnov test to identify the parameters that best reproduce the observed $\log(L_{H\alpha}/L_{UV})$ distribution in each mass bin. The other improvement in W12 was the finer sampling of parameter space. The main conclusion of W12 is that galaxies with the lowest stellar masses have higher-amplitude

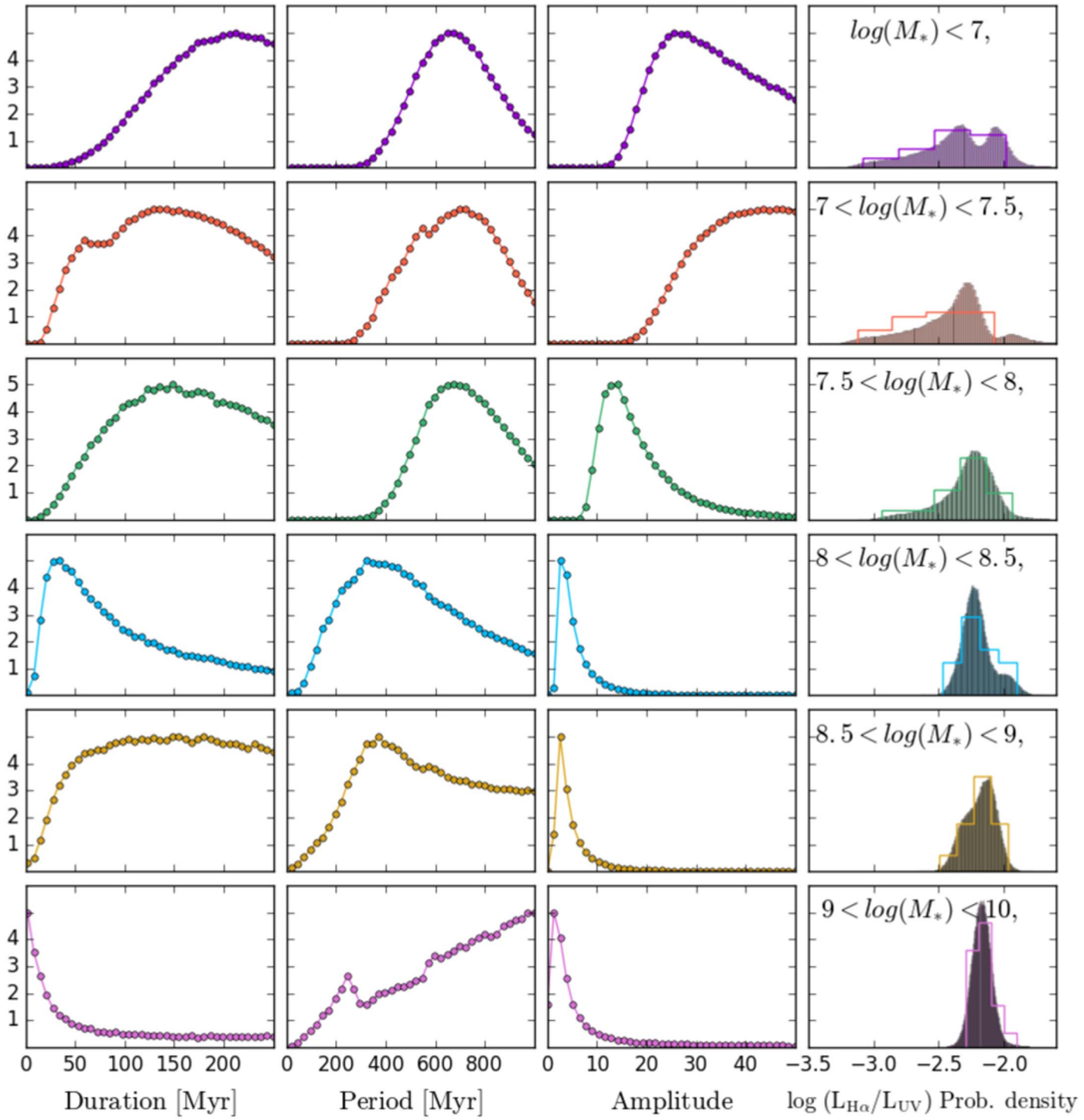


Figure 1. Likelihood functions of duration, period, and amplitude (relative to the baseline), as well as the $\log(L_{H\alpha}/L_{UV})$ distribution of the best-fit models to the observed $\log(L_{H\alpha}/L_{UV})$ distribution for each mass bin, assuming metallicities from Andrews & Martini (2013). The open histograms show the observed sample and the filled histograms show the distribution of the best-fit models.

bursts ($A \sim 30\times$ the baseline rate), relatively long durations ($D \sim$ 30–40 Myr), and long periods ($P = 250$ Myr). The highest mass bins are characterized by almost constant SFRs with an occasional modest burst favoring SF models with short duration ($D \sim 6$ Myr) and modest amplitudes ($A \sim 10$).

In the Appendix, we describe an analysis similar to that of W12, but with three significant improvements to better determine the best parameters of bursty SF. First, we use appropriate (lower) stellar metallicities for the lower-mass galaxies, as W12 used solar metallicities for all galaxies. This should change the predicted $\log(L_{H\alpha}/L_{UV})$ distributions because stars of the same mass at lower metallicity will be hotter and have a larger $\log(L_{H\alpha}/L_{UV})$ ratio. Second, we expand the parameter space, because some of the best-fit parameters in W12 were at the edge of the explored parameter space. Finally, we adopt a probabilistic approach to determine the best SFH parameters. This allows us to fully explore the parameter space, determine the relative merit (the likelihood) of

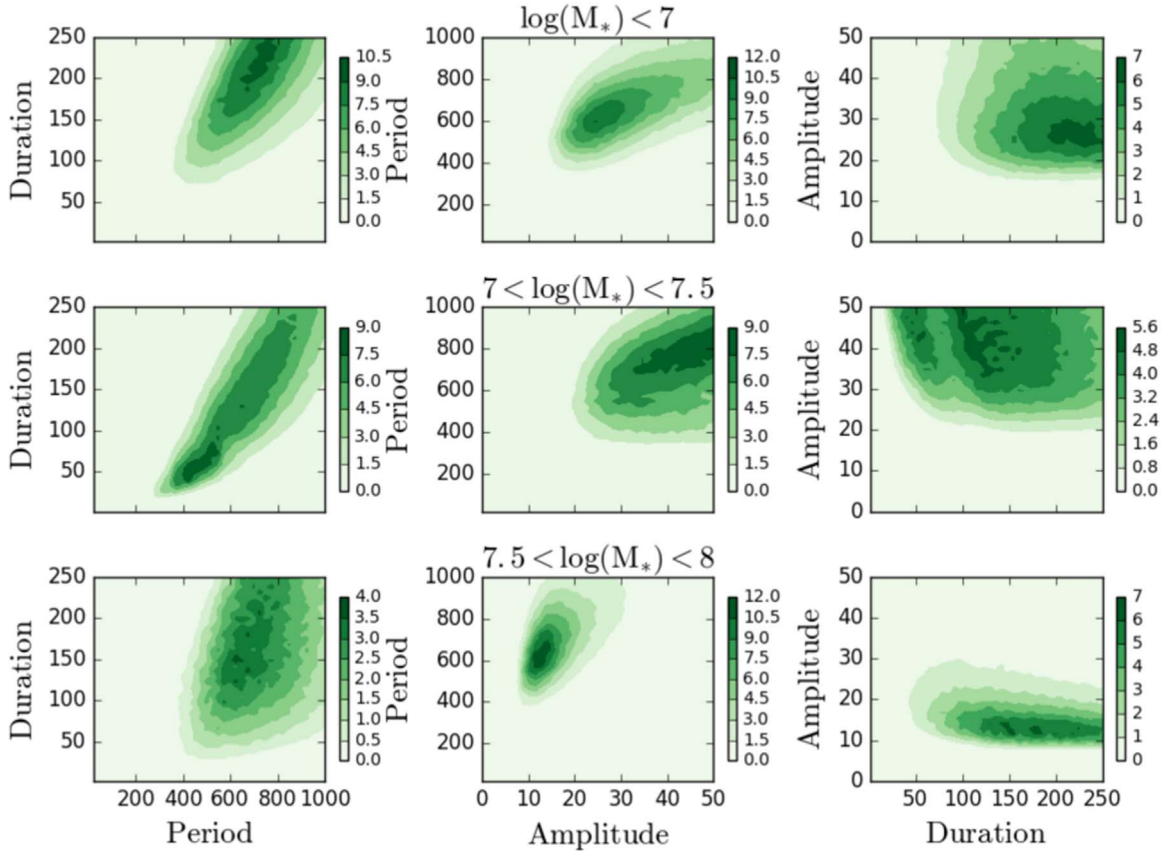


Figure 2. 2D contour plots of (D, P), (P, A), and (A, D). Each row corresponds to a different mass range: $M \leqslant 10^7\,M_\odot$, $10^7 < M \leqslant 10^{7.5}\,M_\odot$, and $10^{7.5} < M \leqslant 10^8\,M_\odot$ from top to bottom. The probability densities are denoted by color bars on the right of each panel. The strong degeneracy in duration and period can be seen for all mass ranges shown here.

each set of parameters, and search for any significant degeneracies between the parameters.

The results of our method are presented in Figure 1, which shows the marginalized likelihood of the duration, period, and amplitude for the six stellar mass ranges defined in Table 2. On the right, the observed $\log(L_{\rm H\alpha}/L_{\rm UV})$ distributions for each mass bin are plotted as unfilled histograms along with the distribution of the best-fit models as filled histograms.

Galaxies with $M \geqslant 10^8\ M_\odot$ have best-fit amplitudes <3, signifying relatively stable star formation histories. However, such low amplitudes are very sensitive to the assumed errors in the observed luminosities and dust extinction corrections. On the other hand, all of the stellar mass bins at $M < 10^8\ M_\odot$ have best-fit amplitudes >15, suggesting that dramatic bursts of star formation are necessary to explain the large spread of $\log(L_{\rm H\alpha}/L_{\rm UV})$ seen in these galaxies.

Our new analysis demonstrates that W12 did not probe the parameter space with the highest likelihood, because the posteriors peak at a period of 500–900 Myr (Figure 1 second column) (where W12 analyzed $P < 250$ Myr). This is important for the duration parameter as well, because it is highly correlated with the period (see below). Thus, the new estimates of duration are considerably larger ($D \sim 40$–250 Myr) than $D \sim 20$ Myr in W12. The estimates of amplitude are uncertain, but broadly agree with the values in W12.

To better understand the degeneracies between the model parameters, we plot the 2D contours of the three lowest mass bins in Figure 2. In the duration–period contour plots, there is a linear degeneracy between period and duration, such that increasing the duration of the burst requires a similar increase in the period.

These degeneracies result in large uncertainties in the marginalized posteriors for both duration and period. Specifically, the burst durations of the low-mass galaxies can be 50 or 250 Myr (or larger). Furthermore, we know that this periodic top-hat model is not accurate in that the star formation does not instantly change and is not truly periodic. Therefore, it is difficult to know whether or not these best-fit parameters reflect the true values of typical duration and period in these galaxies.

4. A New Approach to Characterizing Bursty Star Formation

So far we have reviewed the previous studies and more carefully explored the top-hat periodic SF model of W12 to determine parameters of SFHs based only on the $\log(L_{\rm H\alpha}/L_{\rm UV})$ distribution.

However, two concerns ultimately arise from our new analysis. First, our new probabilistic approach allows us to see that significant degeneracies exist between the model parameters (see Figure 2). This is perhaps not surprising, because there are three parameters fit to a single $\log(L_{\rm H\alpha}/L_{\rm UV})$ distribution. Ultimately, it is necessary to use additional observables to fit complicated star formation histories.

Second, we know that the periodic, top-hat burst model is unphysical, because it requires instantaneous changes in SFR. Indeed, the best-fit model predicts other observable distributions that do not look like those observed. For example, the model predicts a bimodal $\Delta\log(L_{\rm H\alpha})$ distribution at each mass,

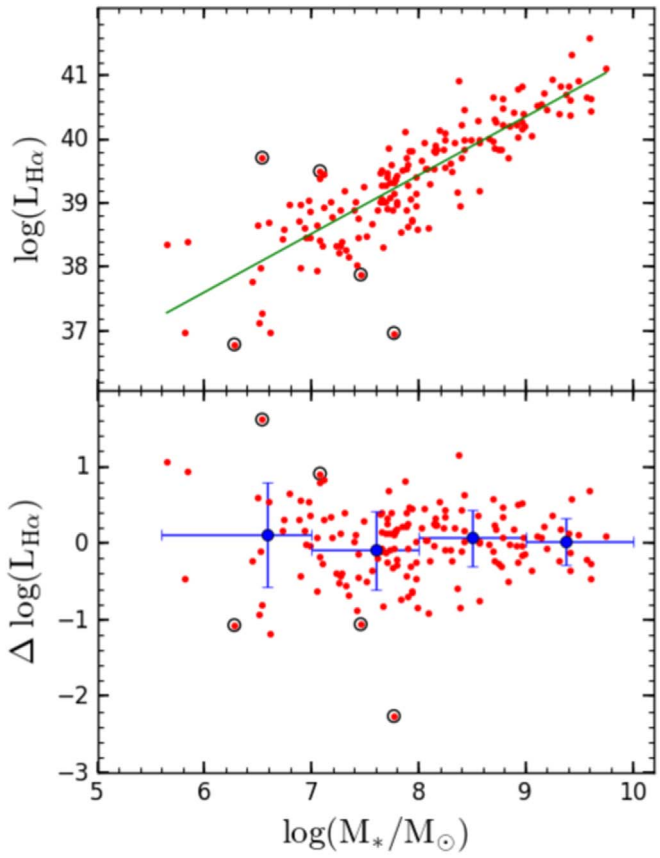


Figure 3. Top: $\log(L_{H\alpha})$ vs. $\log(M_*)$ for the W12 sample (red dots). The correlation between these two observables is known as the star-forming "main sequence." The black circles show outliers in $\log(L_{H\alpha}/L_{UV})$ (either > -1.8 or < -3.4) that are removed from the sample for the subsequent analysis. Bottom: the deviation of $\log(L_{H\alpha})$, $\Delta\log(L_{H\alpha})$, from the linear relation shown by the green line in the top panel. The blue circles are the median in each stellar mass bin. The horizontal error bars denote the stellar mass range of each bin and the vertical error bars are the standard deviation in each bin. The scatter around the mean trend (green line) increases toward lower stellar masses, from 0.3 dex at $\log(M_*) \sim 9.4$ to 0.7 dex at $\log(M_*) \sim 6.6$.

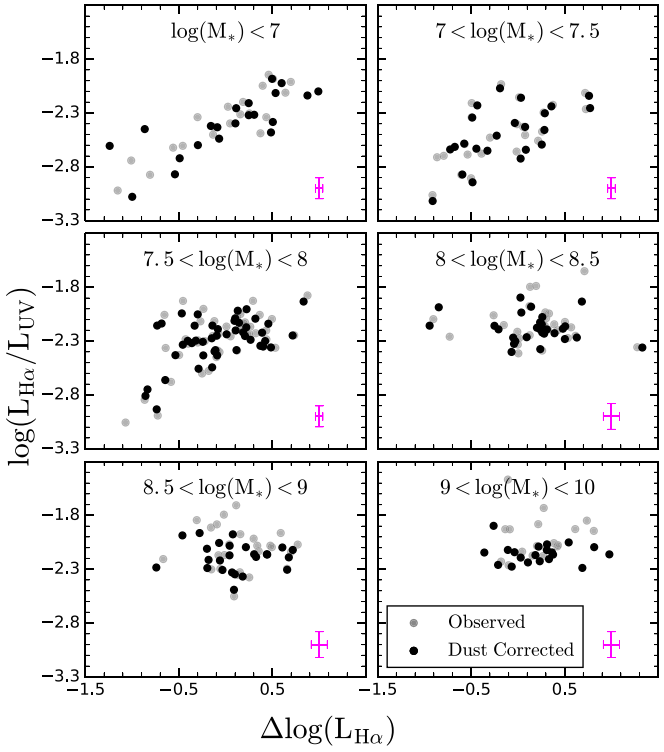


Figure 4. $\log(L_{H\alpha}/L_{UV})$ vs. $\Delta\log(L_{H\alpha})$ for the W12 sample in six different mass ranges. The gray and black points are the observed and dust-corrected values respectively. Representative error bars of 10%–20% in $L_{H\alpha}$ and L_{UV} derived from Lee et al. (2009) are shown in the bottom right of each subplot in magenta. At high stellar mass, the galaxies span a narrow range in $\log(L_{H\alpha}/L_{UV})$. At low mass, the galaxies span a large range in $\log(L_{H\alpha}/L_{UV})$, and $\log(L_{H\alpha}/L_{UV})$ is positively correlated with $\Delta\log(L_{H\alpha})$. This correlations shows that, not only should these two observables be used to determine the properties of bursty star formation, but their two-dimensional distribution should be considered.

rather than the observed distribution, where galaxies are more evenly distributed in $\Delta\log(L_{H\alpha})$, suggesting that the typical galaxy spends a significant fraction of its lifetime near the average SFR, rather than in low and high states.

In this section, we seek to add additional observables to constrain the star formation histories, and we choose a somewhat simpler parameterization in order to focus on the timescales of the transitions from burst to quiescence and back.

4.1. The $L_{H\alpha}$ Distribution

$L_{H\alpha}$ is strongly correlated with stellar mass, M_*, with the scatter around the mean increasing at lower stellar mass (Figure 3). Thus, this distribution contains additional information about the SFH and we should be incorporating the $L_{H\alpha}$ distribution into our analyses of the SFH. Of course, the average of the distribution depends strongly on the stellar mass of the galaxy, and does not give any information about the relative changes in the SFR. We therefore choose to subtract the trend of $\log(L_{H\alpha})$, defining this as $\Delta\log(L_{H\alpha})$, plotted in Figure 3. The value of $\Delta\log(L_{H\alpha})$ tells us a galaxy's (nearly instantaneous) SFR, relative to the average, and the width of the distribution translates to a maximum burst amplitude, relative to the average. But it is particularly useful when examined in conjunction with $\log(L_{H\alpha}/L_{UV})$, because $\log(L_{H\alpha}/L_{UV})$ gives us time information, indicating how quickly (or how recently) a given galaxy has increased or decreased its SFR.

In Figure 4, we show the location of the W12 galaxies in the $\Delta\log(L_{H\alpha})$–$\log(L_{H\alpha}/L_{UV})$ plane in bins of stellar mass. The gray and black points correspond to the observed and dust-corrected values, respectively. Note that the dust corrections are very small and do not change the shape of the correlations seen in Figure 4. The representative errors of 10%–20% corresponding to $L_{H\alpha}$ and L_{UV} are shown in the bottom right of each subplot in magenta. These errors are derived from the typical dispersion in dust attenuation as a function of absolute B-band magnitude, as reported in Lee et al. (2009). Specifically, galaxies in our sample span $-18.4 < M_B < -13$, for which $L_{H\alpha}$ is uncertain by 10% for stellar masses below $10^8\ M_\odot$ and 20% otherwise, and L_{UV} is uncertain by 20% in the entire sample. As indicated before, the lower-mass galaxies span a larger range in $\Delta\log(L_{H\alpha})$ and $\log(L_{H\alpha}/L_{UV})$. But what is most informative is that the two measurements are highly correlated in galaxies with $\log(M_*) < 8$. That is, we are not just fitting to the 1D distributions of $\Delta\log(L_{H\alpha})$ and $\log(L_{H\alpha}/L_{UV})$, but also considering the correlations between the two.

We emphasize that we would like to use these distributions to infer SFHs of all of the galaxies in each mass bin. In order to do that, it is important to be sure that all galaxies in the bin are

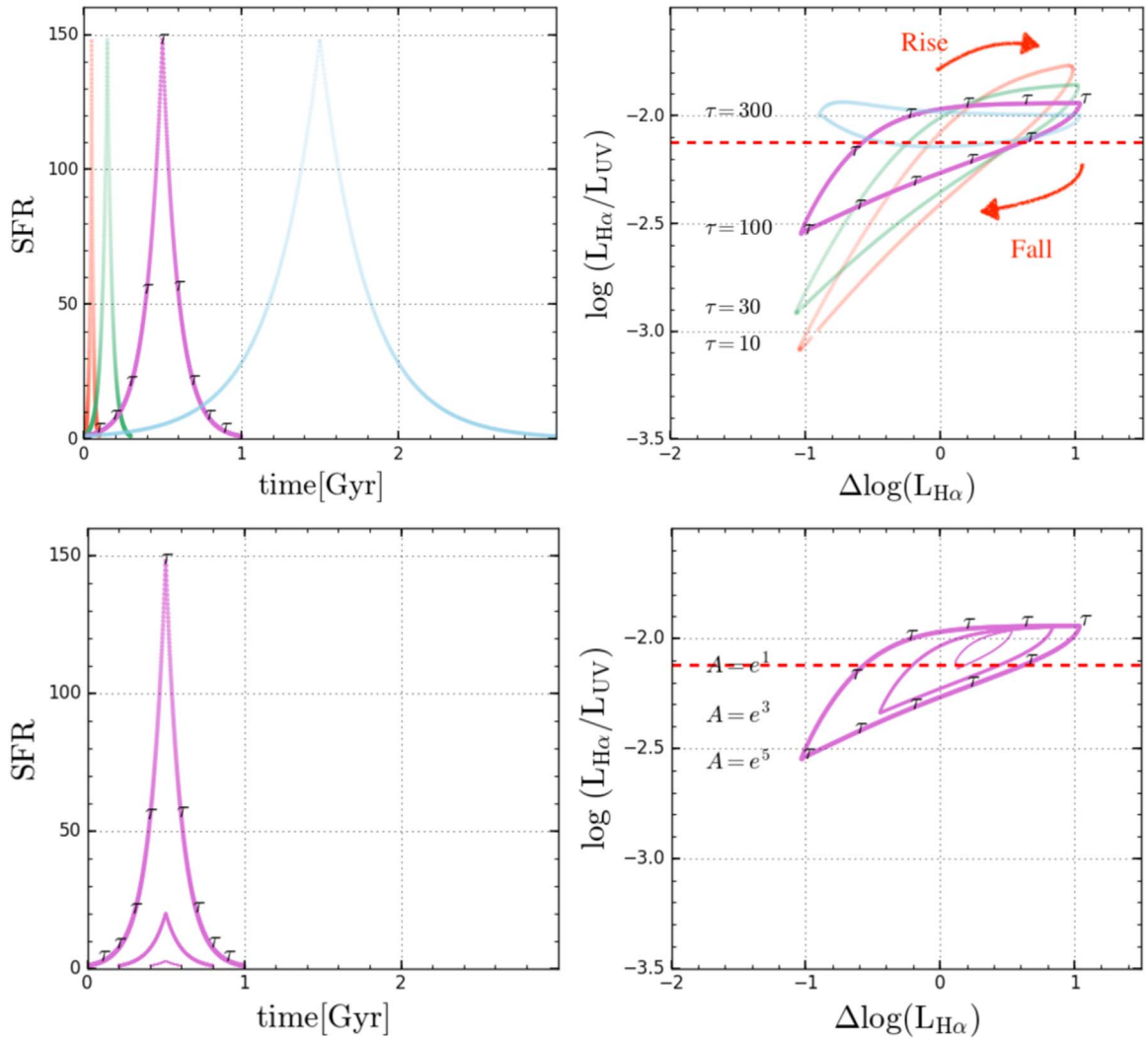


Figure 5. Top left: SF history of four exponentially rising and declining bursts with varying $\tau = 10$, 30, 100, 300 Myr and a fixed amplitude of $A = e^5 = 148$ (or equivalently a duration of 5τ). Top right: the associated $\log(L_{H\alpha}/L_{UV})$–$\Delta\log(L_{H\alpha})$ for the SFHs in the left panel. We highlight the $\tau = 100$ Myr model, and place "τ" symbols at intervals of $\Delta t = \tau$. The equilibrium value (assuming a constant SFR) of $\log(L_{H\alpha}/L_{UV}) = -2.12$ is marked with a red dashed line. As τ decreases, the slope of $\log(L_{H\alpha}/L_{UV})$–$\Delta\log(L_{H\alpha})$ gets steeper. Bottom: same as top panels except for models with fixed $\tau = 100$ Myr and varying amplitudes of $A = e^1$, e^3, and e^5. The slope of $\log(L_{H\alpha}/L_{UV})$–$\Delta\log(L_{H\alpha})$ is unchanged but the points span smaller $\Delta\log(L_{H\alpha})$ ranges. Note that in an exponential model, the galaxies spend equal amounts of time in equal intervals of $\Delta\log(L_{H\alpha})$.

behaving in a similar manner, and that these measurements represent random samples of the same SFHs. One particular point of concern is the possibility that subsets of galaxies permanently reside above the SF main sequence ($\Delta\log(L_{H\alpha}) > 0$) and others reside below it ($\Delta\log(L_{H\alpha}) < 0$), for example, because of different average gas infall rates in different environments. If that were the case, there would be no difference in the $\log(L_{H\alpha}/L_{UV})$ ratio of galaxies above and below the main sequence. However, Figure 4 shows a strong correlation between $\log(L_{H\alpha}/L_{UV})$ and $\Delta\log(L_{H\alpha})$ in low-mass galaxies ($\log(M_*) < 8$). Specifically, galaxies that have higher than average SFRs have $\log(L_{H\alpha}/L_{UV}) \sim -2.2$, indicative of constant or rising SFRs, and galaxies that have lower than average SFRs have $\log(L_{H\alpha}/L_{UV}) < -2.5$, indicative of declining SFRs. This indicates that all of the galaxies in a given stellar mass bin have similar star formation histories.

4.2. The Exponential Burst Model

The SF histories of galaxies are not periodic, top-hat bursts, and are instead stochastic in nature. Because such simple models do not represent the actual SFHs, it is difficult to ascertain whether the best-fit parameters of the model are physically meaningful. Therefore, we are not particularly interested in confining ourselves to a highly parameterized, unphysical SFH. As discussed above, the amplitude of the bursts can be determined from the width of the $L_{H\alpha}$ distribution. What remains unknown are the timescales for the burst and quench phases.

We have chosen to parameterize the rise and decline of a burst as an exponential in time such that

$$\mathrm{SFR}(t) = \begin{cases} e^{t/\tau}, & \text{if } 0 \leqslant t < D \\ e^{-(t-2D)/\tau}, & \text{if } D < t \leqslant 2D \end{cases} \quad (1)$$

where τ is the e-folding time, representing the typical timescale for significant change in the SFR. Part of our motivation for choosing an exponential burst model comes from the SFHs in some hydrodynamical simulations. For example, star formation histories from the FIRE-2 simulations (Hopkins et al. 2018)

indicate individual bursts with exponential rises and declines (see Figure 7). For the sake of simplicity, we assume that the rise and decline in the galaxies' SFR are both described with the same e-folding time, τ. With such a parameterization, we can target the timescale, independent of the absolute amplitude of the burst. Also, the SFHs are assumed to be periodic in repeating forms of Equation (1).

In the top left panel of Figure 5, we plot model star formation histories with $\tau = 10$, 30, 100, 300 Myr and an amplitude of $A = e^5 = 148$ (or equivalently a duration of 5τ). In the top right panel, we plot the associated $\log(L_{\rm H\alpha}/L_{\rm UV})$ versus $\Delta\log(L_{\rm H\alpha})$. Here $\Delta\log(L_{\rm H\alpha})$ is calculated as $\log(L_{\rm H\alpha})$ from the synthetic stellar population model of Bruzual & Charlot (2003) (BC03) subtracted from the value of $\log(L_{\rm H\alpha})$ for a constant SFR that is equal to the average SFR of the exponential model.

The $\tau = 100$ Myr model is highlighted in purple to demonstrate the motion of a bursty galaxy in this observable space. We note that the observable ratios are dependent on previous star formation. Thus, the plotted ratios are for a burst preceded by identical bursts. Obviously, as the galaxy SFR rises (burst phase), $\Delta\log(L_{\rm H\alpha})$ increases and the galaxy moves to the right in the plot. As the galaxy SFR declines (quench phase), $\Delta\log(L_{\rm H\alpha})$ decreases and the galaxy moves to the left in the plot. The motion in $\log(L_{\rm H\alpha}/L_{\rm UV})$ is more complicated, depending on the timescale of change in SFR, τ. For long timescales, $\tau > 300$ Myr, both of the luminosities in the log $(L_{\rm H\alpha}/L_{\rm UV})$ ratio have time to react and accurately trace the SFR. Therefore, $\log(L_{\rm H\alpha}/L_{\rm UV})$ does not change significantly as the SFR declines. However, if $\tau < 300$ Myr, $L_{\rm UV}$ lags $L_{\rm H\alpha}$ in tracing the decline in SFR, and $\log(L_{\rm H\alpha}/L_{\rm UV})$ will decrease as $\Delta\log(L_{\rm H\alpha})$ decreases. As τ decreases, the slope of the curves increases. However, the slope saturates at $\sim$0.6 for $\tau <$ 30 Myr. Therefore, examination of galaxies in this observable space is only useful for identifying changes in SFR on timescales of $30 < \tau < 300$ Myr. The bottom panels of Figure 5 indicate the SFHs and associated $\log(L_{\rm H\alpha}/L_{\rm UV})$–$\Delta\log(L_{\rm H\alpha})$ relation of three exponential burst models for the case where the e-folding time (τ) is fixed at 100 Myr and the amplitudes are allowed to vary with $A = e^1$, e^3, and e^5. The model with largest amplitude (e^5) spans a larger part of the $\Delta\log(L_{\rm H\alpha})$ axis, while the slope remains unchanged in all three models.

We note that in the exponential model, the galaxies are evenly spread in $\Delta\log(L_{\rm H\alpha})$ during the transition from quench to burst and vice versa. In contrast, the periodic top-hat burst model results in most galaxies having two $\Delta\log(L_{\rm H\alpha})$ values, with few points in between. The observed ratios are roughly evenly distributed in $\Delta\log(L_{\rm H\alpha})$, similar to the exponential model.

4.3. Results

In Figure 6, we again plot the W12 data in this log $(L_{\rm H\alpha}/L_{\rm UV})$–$\Delta\log(L_{\rm H\alpha})$ plane. As mentioned above, the data clearly show that even though the SFR of the high-mass galaxies changes significantly, the $\log(L_{\rm H\alpha}/L_{\rm UV})$ ratio does not. In the context of our exponential burst model, this indicates that the changes in SFR are slow, with $\tau \gtrsim 300$ Myr. At low mass, however, $\log(L_{\rm H\alpha}/L_{\rm UV})$ is highly correlated with $\Delta\log(L_{\rm H\alpha})$, suggesting that the SFRs change rapidly, with $\tau \lesssim$ 100 Myr.

Table 1
Best-fit Values of the Exponential Burst Parameters: the e-folding Time (τ) and the Amplitude (A) for Six Different Stellar Mass Bins

$\log(M_*)$	τ (Myr)	A
$\leqslant$7	<30	100
7–7.5	<30	100
7.5–8	30	30
8–8.5	100	10
8.5–9	300	10
9–10	>300	10

In Figure 6, we also plot the tracks (cyan) for values of τ and A that best match the data in each mass range. A summary of these values is also reported in Table 1 for a better comparison. We note that we do not perform any probabilistic analysis to determine the best-fit exponential models of each mass bin. Due to systematic uncertainties (e.g., extinction correction, metallicity, stellar models, escape fraction), the models may not precisely reproduce the data. We therefore determine (by eye) approximate model parameters that reproduce the slope and breadth of the data in the observed $\log(L_{\rm H\alpha}/L_{\rm UV})$ versus $\Delta\log(L_{\rm H\alpha})$ plane. A 10%–20% observational uncertainty is added to the model (in both $L_{\rm H\alpha}$ and $L_{\rm UV}$) to mimic the true uncertainty in the data, as discussed in Section 4.1. The approximate values of τ and A are written in the bottom right of each subplot. Two trends are clear with mass. First, the amplitudes—the ratio of maximum to minimum SFR (or $L_{\rm H\alpha}$) in galaxies of the same mass—increase toward lower mass ($A \sim 10$ for $\log(M_*) > 9$ to $A \sim 100$ for $\log(M_*) < 7.5$). Second, the timescale for changes in SFR (τ) decreases with decreasing stellar mass, with $\tau > 300$ Myr for $\log(M_*) > 8.5$ and $\tau < 30$ Myr for $\log(M_*) < 7.5$.

We note that, within the scatter, the slopes of the data in the $\log(L_{\rm H\alpha}/L_{\rm UV})$–$\Delta\log(L_{\rm H\alpha})$ plane are roughly the same for all galaxies with $\log(M_*) > 8.5$ (slope $\sim$0) and for all galaxies with $\log(M_*) < 7.5$ (slope $\sim$0.6). As noted above, the log $(L_{\rm H\alpha}/L_{\rm UV})$ ratio is most useful for identifying changes in SFR on timescales of $\tau \sim 100$ Myr. Thus, it appear that the stellar mass of $\log(M_*) \sim 8$ (at $z = 0$) represents the critical mass at which the timescale for change in SFR is approximately $\tau \sim 100$ Myr. This is an observational result, and is true regardless of the physical mechanisms involved.

It is noteworthy that Meurer et al. (2009) looked at the burstiness in the $\log(L_{\rm H\alpha}/L_{\rm UV})$–$\Sigma_{\rm H\alpha}$ plane, which is very similar to the observables we analyze (replacing $\Delta\log(L_{\rm H\alpha})$ with Hα surface brightness). In addition, they used Gaussian bursts and gasps, which are exponential at the beginning and end, similar to our model bursts. Indeed, their models show a similar behavior in $\log(L_{\rm H\alpha}/L_{\rm UV})$–$\Sigma_{\rm H\alpha}$ to our exponential models, especially in the gasp phase. However, their models have a very significant difference from ours—they assume a low-level, constant SFR when not in a burst or gasp. This assumption requires that the galaxies have high $\log(L_{\rm H\alpha}/L_{\rm UV})$ before a new burst/gasp starts. Ultimately, this assumption makes it impossible to reproduce the observed $\log(L_{\rm H\alpha}/L_{\rm UV})$–$\Sigma_R$ (optical surface brightness) distribution of the galaxies, because it cannot produce galaxies with both low $\log(L_{\rm H\alpha}/L_{\rm UV})$ (which can be produced only with a quick downturn in star formation) and low Σ_R (which cannot be produced with a quick downturn in star formation, if one assume that galaxies start with a high Σ_R). Meurer et al. (2009) therefore concluded that the SFH cannot fully

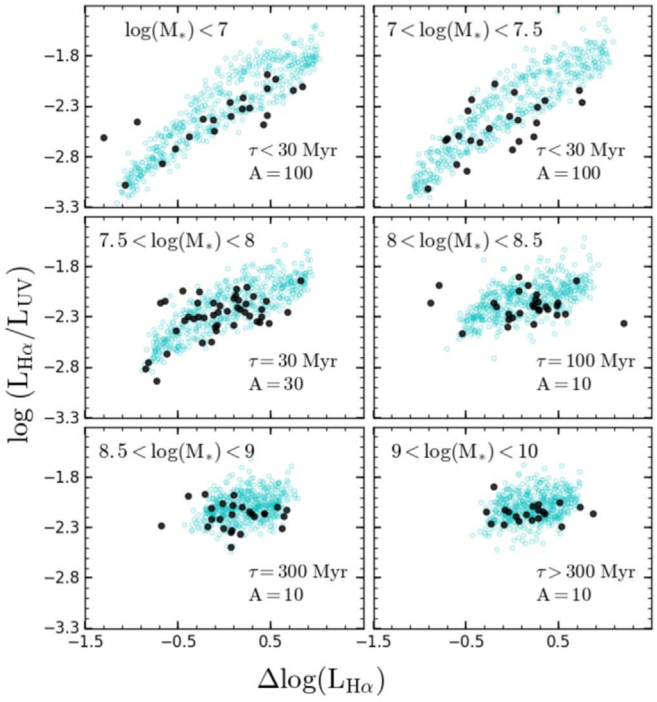


Figure 6. Location of modeled galaxies in the $\log(L_{H\alpha}/L_{UV})$–$\Delta\log(L_{H\alpha})$ plane (cyan circles), undergoing periodic, exponential bursts of SF with different timescales, τ, and amplitude, A, sorted by mass. Note that the timescales in the two lowest mass bins read $\tau < 30$ Myr because the slope of the relation does not change below that timescale. We used $\tau = 10$ Myr for these two mass bins. A 10%–20% systematic uncertainty corresponding to errors reported in Figure 4 is added to each luminosity to mimic the observational uncertainties. The black points are the W12 observed data. The best-fit values of τ and A are written in the bottom right of each subplot. The timescale for changes in SFR increases with increasing stellar mass.

explain the low $\log(L_{H\alpha}/L_{UV})$ ratio in galaxies of low surface brightness.

Within the framework of our model, however, these galaxies of low surface brightness with low $\log(L_{H\alpha}/L_{UV})$ are naturally explained by low-mass galaxies (which typically have low optical surface brightness, de Jong & Lacey 2000) with rapidly declining SFR. Ultimately, we believe that our splitting of the sample into different mass bins (which, on average, have different optical surface brightnesses and different timescales) and our assumption that no constant, baseline SFR is required in our models allow us to naturally explain the $L_{H\alpha}$ and L_{UV} distributions with SFHs alone.

There have also been investigations of the properties of bursty galaxies at moderate redshift ($0.4 < z < 1$) in CANDELS GOODS-N by looking at $L_{H\beta}/L_{UV}$ (Guo et al. 2016). In that paper, they observed a decreasing trend of $L_{H\beta}/L_{UV}$ toward low masses similar to the local sample of W12. They found a correlation between $L_{H\beta}/L_{UV}$ and the $L_{H\beta}$-derived specific SFR (sSFR) of their sample, as evidence for bursty star formation. They conclude that the galaxies in their sample are also bursty. But the bursty SF occurs below a higher mass threshold than at lower redshift ($M_* < 10^9\ M_\odot$ compared to $M_* < 10^8\ M_\odot$ at low redshift).

5. Discussion

So far, we have constrained the parameters of bursty star formation by looking at the position of the observed galaxies in the $\log(L_{H\alpha}/L_{UV})$–$\Delta\log(L_{H\alpha})$ plane. We used an exponential SF model to reproduce the $\log(L_{H\alpha}/L_{UV})$–$\Delta\log(L_{H\alpha})$ distribution and found the best-fit timescales and amplitudes of bursts as a function of stellar mass.

In this section, we compare our predictions with hydrodynamical simulations. We also consider the effect of stochastic IMF sampling within our $\log(L_{H\alpha}/L_{UV})$–$\Delta\log(L_{H\alpha})$ framework. Finally, we discuss the effect of the escape fraction of ionizing photons and dust correction uncertainties.

5.1. Comparison with Hydrodynamical Simulations

Many high-resolution hydrodynamical simulations of dwarf galaxies implement stellar feedback and supernovae, resulting in bursty SF (Governato et al. 2010; Domínguez et al. 2015). The effects of bursty SFHs on sample selection and interpretation of observables have been extensively investigated by Domínguez et al. (2015) using the SFHs from hydrodynamical simulations. The FIRE-1 and FIRE-2 (Feedback in Realistic Environments) simulations (Hopkins et al. 2014, 2018) implement prescriptions for a variety of stellar and supernovae feedback processes that are not tuned to reproduce observed scaling laws. Galaxies of different stellar masses are simulated, from dwarfs to Milky Way-like systems, reproducing the empirical relations between galactic observables, such as the stellar mass–halo mass relation, the mass–metallicity relation, etc. Due to their high resolution and focus on stellar/supernovae feedback, the FIRE-2 simulations are well suited for our goal of studying burstiness in dwarf galaxies.

Sparre et al. (2017) studied $L_{H\alpha}$ and L_{UV} as proxies of the SFR averaged over 10 and 200 Myr and found that the FIRE-1 simulations (Hopkins et al. 2014) are more bursty than observed galaxies. Specifically, the FIRE-1 galaxies display a larger range in $L_{H\alpha}/L_{UV}$ than the observed galaxies of W12 in the range $8 < \log(M_*[M_\odot]) < 9.5$. The FIRE-2 simulations (Hopkins et al. 2018) used improved numerical accuracy, resulting in more accurate treatments of cooling and recombination rates, gravitational force softening, and numerical feedback coupling. However, the core physics is the same as in FIRE-1. These enhancements lead FIRE-2 to produce more realistic bursts of SF. FIRE-2 also contains a larger sample of galaxies than the previous version, allowing a better understanding of variations in galaxy properties. The detailed properties of the individual simulations can be found in El-Badry et al. (2018) and Hopkins et al. (2018).

We use the star formation histories of the FIRE-2 galaxies, which span a similar range in stellar mass over their last 2 Gyr (corresponding to $z = 0.15$–0) to the W12 mass range, to determine their location and evolution in the $\log(L_{H\alpha}/L_{UV})$ versus $\Delta\log(L_{H\alpha})$ plane, and compare them with the observed W12 sample.

Figure 7 shows three examples of star formation histories of FIRE-2 simulated galaxies, whose name and stellar mass at $z = 0$ are written at the top left of each panel. We specifically chose galaxies with a different range of stellar masses. The galaxies have bursts of SF with a short time at the peak. We see that galaxies rise and decline quickly in a roughly exponential form. For illustration purposes, we marked some of these exponential bursts in Figure 7 in magenta and fit Equation (1) to individual bursts (using a curve fit Scipy package from Python) in order to find an estimate of rising and falling timescales for these galaxies. Based on this simple fitting, all three of these galaxies indicate timescales of $\tau < 15$ Myr.

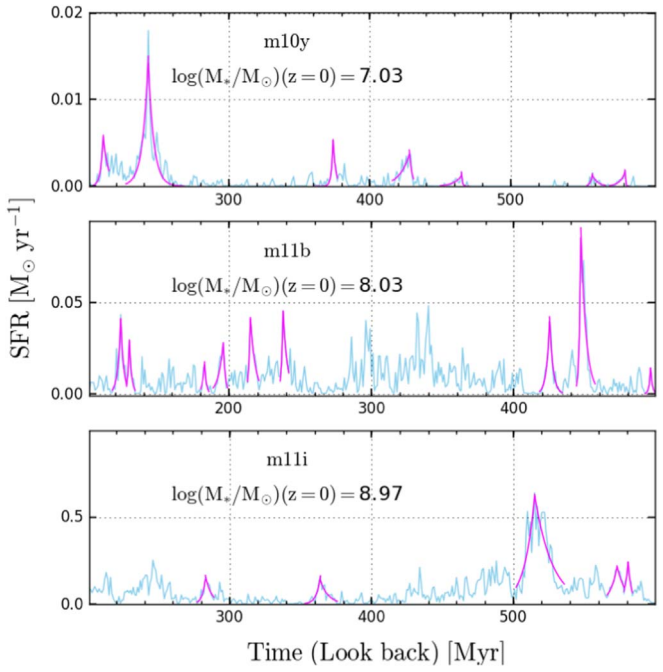


Figure 7. Star formation histories of three galaxies in the FIRE-2 simulations (Hopkins et al. 2018) (cyan). The name and stellar mass of the galaxies at $z = 0$ are labeled at the top left of each panel. The magenta lines are the best-fit exponential functions to the individual bursts. The marked bursts all have e-folding timescale of τ below 15 Myr.

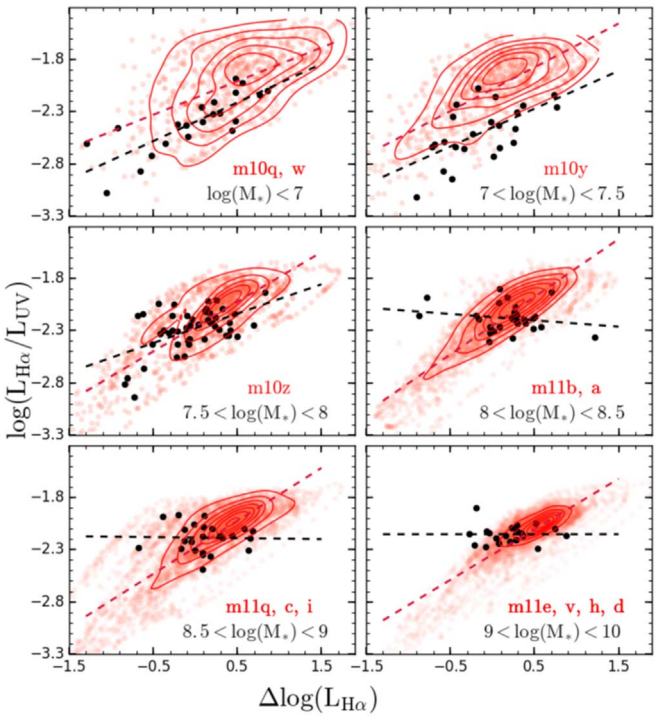


Figure 8. $\log(L_{H\alpha}/L_{UV})$ vs. $\Delta\log(L_{H\alpha})$ for FIRE-2 simulated galaxies (red circles and contours) and W12 data for local galaxies (black circles). The FIRE-2 galaxies are selected to be within the specified mass range at $z = 0$. The names of the FIRE-2 galaxies are labeled in red. Red and black dashed lines are the best-fit lines to the simulated and observed galaxies, respectively. We note that a significant fraction of the lowest mass galaxies ($\log(M_*) < 7$) exhibit no star formation for long periods of time and would lie off to the bottom left of the plot. The simulated galaxies all span a similar range in $\Delta\log(L_{H\alpha})$ to the observed galaxies, suggesting similar burst amplitudes. However, the simulated galaxies at higher mass show a positive correlation between $\log(L_{H\alpha}/L_{UV})$ and $\Delta\log(L_{H\alpha})$ that is not seen in the observed galaxies, suggesting that the timescale for change in SFR is too short in simulated galaxies. This is also evident from the slope of the red dashed lines in these mass bins.

The L_{UV} and $L_{H\alpha}$ fluxes are derived by convolving the simulated star formation histories over the last 2 Gyr with the Hα and UV luminosity evolution from models of single stellar populations (Bruzual & Charlot 2003) with stellar metallicity of $0.2\,Z_\odot$. This is the same method as described for our parameterized bursty star formation in the Appendix. We note that in the low-mass galaxies in which we are most interested, the vast majority of stars are formed in situ and not acquired in mergers (Fitts et al. 2018). Furthermore, most of the mergers happened at $z > 3$, so the accreted stars are old and will not affect the calculations of $L_{H\alpha}$ or L_{UV} (Fitts et al. 2018) at late times.

In Figure 8 we plot $\log(L_{H\alpha}/L_{UV})$ versus $\Delta\log(L_{H\alpha})$ for FIRE-2 simulated galaxies, where the color indicates the density of points at any location on the plot. Overlaid is the W12 observed sample in black circles. We calculate the median $L_{H\alpha}$ from the linear fit to the $L_{H\alpha}$ versus mass relation for FIRE-2 galaxies and subtract this to determine $\Delta\log(L_{H\alpha})$. The names of the plotted FIRE-2 galaxies are labeled in red. One common feature that can be seen in both the observations and simulation is that the low-mass galaxies exhibit a larger spread in the $\log(L_{H\alpha}/L_{UV})$ versus $\Delta\log(L_{H\alpha})$ space while the spread becomes smaller at higher masses. Nonetheless, there are some discrepancies between them.

As mentioned before, the observations show no relation between $L_{H\alpha}/L_{UV}$ and $\Delta\log(L_{H\alpha})$ above $10^8\,M_\odot$, but show a strong correlation below $10^8\,M_\odot$. This is seen in the slope of the best-fit lines to the data in Figure 8. However, the simulated galaxies show a strong correlation, with a similar slope, at all stellar masses (red dashed line in Figure 8). Comparison with our exponential burst models (Section 4.2) on the FIRE-2 galaxies indicates that the bursts/quenches have e-folding times of τ below 30 Myr in the simulated galaxies at all masses. However, the W12 data suggest that the e-folding time increases toward higher stellar masses. In particular, at stellar masses above 10^8, the FIRE-2 simulations have far faster bursts ($\tau < 30$ Myr) than the timescales implied by the observation of real galaxies ($\tau \gtrsim 300$ Myr). We therefore suggest that the rapid bursts in the FIRE-2 simulations of more massive galaxies should be examined to determine possible shortcomings in the existing feedback prescriptions.

We note here that although the $\log(L_{H\alpha}/L_{UV})$ and $\Delta\log(L_{H\alpha})$ distributions are similar to those in the observed galaxies, it is the examination of the two-dimensional space of $\log(L_{H\alpha}/L_{UV})$–$\Delta\log(L_{H\alpha})$ that allows us to recognize that the timescales for the bursts in more massive galaxies may not be correct.

One other difference between the simulation and observation that becomes more significant at masses below $10^{7.5}M_\odot$ is that the simulation produces larger $\log(L_{H\alpha}/L_{UV})$ than what is observed in real galaxies. We address this offset in Section 5.3.

We choose galaxy "m11b," with stellar mass of $10^8\,M_\odot$ at $z = 0$, as an example to demonstrate the effect of change in SFR on the $\log(L_{H\alpha}/L_{UV})$–$\Delta\log(L_{H\alpha})$ relation. In Figure 9, we plot a 50 Myr segment of the recent SFH of this galaxy and mark each Myr in a color gradient from dark blue to dark red as the time advances, as is shown on the left plot. The SFH at each point is averaged over its last 3 Myr because it takes about 3 Myr for $L_{H\alpha}$ to react to the change in SFR. On the right panel, we plot the $\log(L_{H\alpha}/L_{UV})$–$\Delta\log(L_{H\alpha})$ associated with the

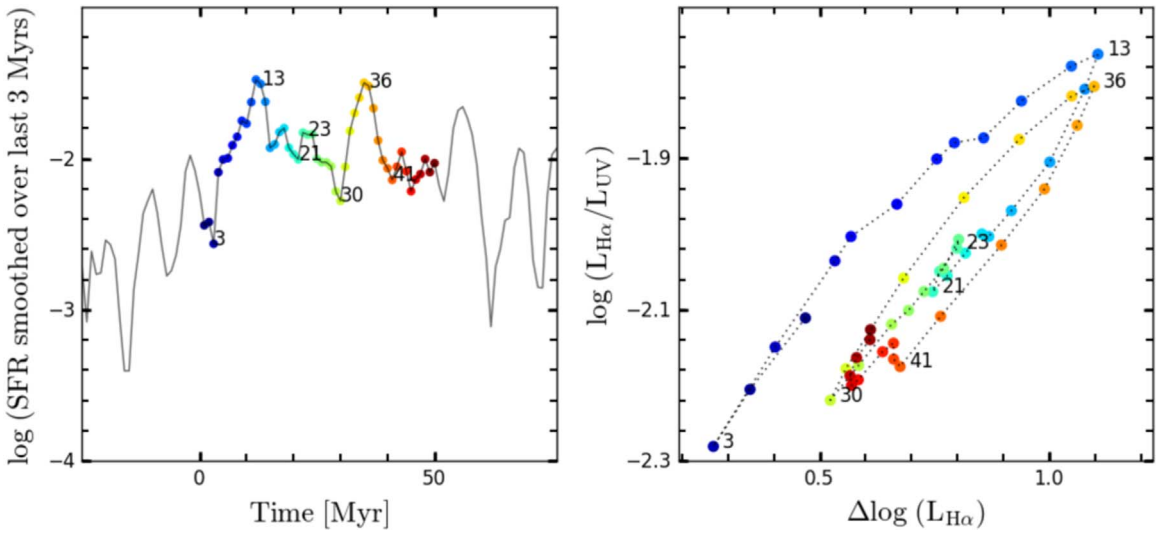


Figure 9. Left: the SFH smoothed over the last 3 Myr for a 50 Myr segment of the recent SFH in galaxy "m11b" with 10^8 $M_\odot$ stellar mass at present ($z = 0$). Right: $\log(L_{H\alpha}/L_{UV})$ vs. $\Delta\log(L_{H\alpha})$ associated with the original (unsmoothed) SFH on the left panel. Colors and numbers represent the same star formation time on both panels. It is clear that $\log(L_{H\alpha}/L_{UV})$–$\Delta\log(L_{H\alpha})$ traces the change in SFR when SFR is smoothed over the last 3 Myr. As star formation rises and declines, it moves diagonally from bottom left to top right and back in the $\log(L_{H\alpha}/L_{UV})$–$\Delta\log(L_{H\alpha})$ plane respectively.

original (unsmoothed) SFH, for which the colors represent the corresponding time on the left panel of the same color. When the SFR begins to rise, the galaxy moves in the log $(L_{H\alpha}/L_{UV})$–$\Delta\log(L_{H\alpha})$ plane from bottom left to top right (3 to 13, 21 to 23, 30 to 36 Myr). When the SFR declines quickly, the galaxy moves back toward the bottom left (13 to 21, 23 to 30, 36 to 41 Myr). Moreover, the larger changes in SFR give rise to larger changes in the $\log(L_{H\alpha}/L_{UV})$–$\Delta\log(L_{H\alpha})$ plane (compare the large decline from 36 to 41 Myr to the smaller decline from 23 to 30 Myr). This behavior is consistent with the predictions from our model.

5.2. Stochastic IMF Sampling

So far we have discussed the luminosity distributions from the perspective of bursty star formation, assuming that the IMF is well sampled in all galaxies at all SFRs. However, it may be the case that stars form in a stochastic manner such that low-mass galaxies with a limited amount of gas form massive stars less frequently. Thus, it may not be appropriate to assume a fully sampled mass function in low-mass galaxies with low SFRs. This will result in a deficit of very high-mass stars, and can significantly change the $\log(L_{H\alpha}/L_{UV})$ and $\Delta\log(L_{H\alpha})$ distributions, even in a galaxy with a constant SFR. If this effect is large, it can incorrectly cause us to assume that a galaxy is undergoing bursty star formation.

Stars are born in clusters, and the distribution of clusters is called the initial cluster mass function (ICMF). The ICMF is typically modeled as a power law, and observations suggest a slope of 2 (Zhang & Fall 1999; Lada & Lada 2003; Fall et al. 2009). Clusters of different masses are formed according to the probability given by the ICMF. Then, stars in each cluster are formed according to the probability given by the ISMF.

Because some studies have indicated that IMF sampling can explain some of the observed $\log(L_{H\alpha}/L_{UV})$ distributions, we attempt here to model stochastic IMF sampling in the W12 galaxies. SLUG (Stochastically Lighting Up Galaxies, da Silva et al. 2012, 2014) is a code that considers stochastic sampling of both the ICMF and then the ISMF to determine the spectrum of star-forming galaxies. We use SLUG to determine the effects

Table 2
Stellar Metallicities Used in Models

Stellar Mass $\log(M/M_\odot)$	Measured Z[a] ($Z_\odot$)	Model Z[b] ($Z_\odot$)
⩽7	N/A	0.2
7–7.5	N/A–0.10	0.2
7.5–8	0.10–0.17	0.4
8–8.5	0.17–0.31	0.4
8.5–9	0.31 –0.46	0.4
9–10	0.46 – 0.70	0.4

Notes.
[a] Measured gas-phase metallicity for each stellar mass bin in Andrews & Martini (2013).
[b] Closest stellar metallicity model in Bruzual & Charlot (2003). Note that we use 0.4 $Z_\odot$ for $\log(M_*) = 7.5$–8 (instead of 0.2 $Z_\odot$) in order to fit the observed $\log(L_{H\alpha}/L_{UV})$ distribution.

of ICMF and ISMF stochastic sampling and thus to determine whether poor sampling of the high-mass ends is responsible for the large scatter in $\log(L_{H\alpha}/L_{UV})$ that we observe in low-mass galaxies. We use stellar metallicities from Table 2, assume a power-law ICMF with a slope of $\beta = 2$, and use Padova stellar tracks with thermally pulsing asymptotic giant branch stars and a Chabrier ISMF. In each mass bin, we use the median $L_{H\alpha}$ of all galaxies to determine a typical SFR in that mass bin, assuming the conversion of Kennicutt (1998). The SLUG code takes the input (constant) SFR and stochastically produces stars, outputting spectral energy distributions (SEDs) every 5 Myr. We assume that all ionizing photons result in a photoionization, and calculate the resulting $L_{H\alpha}$ based on case-B recombination. We determine the $\Delta\log(L_{H\alpha})$ distribution by subtracting the median from the $L_{H\alpha}$ distribution.

In Figure 10, red circles are the output SLUG data and black circles are the W12 observed data. In this figure, we show the evolution of galaxies with constant SFR in the $\log(L_{H\alpha}/L_{UV})$ versus $\Delta\log(L_{H\alpha})$ plane due to stochastic formation of massive stars. When high-mass stars are abundant, the galaxy is high in both $\log(L_{H\alpha}/L_{UV})$ and $\Delta\log(L_{H\alpha})$. When high-mass stars are

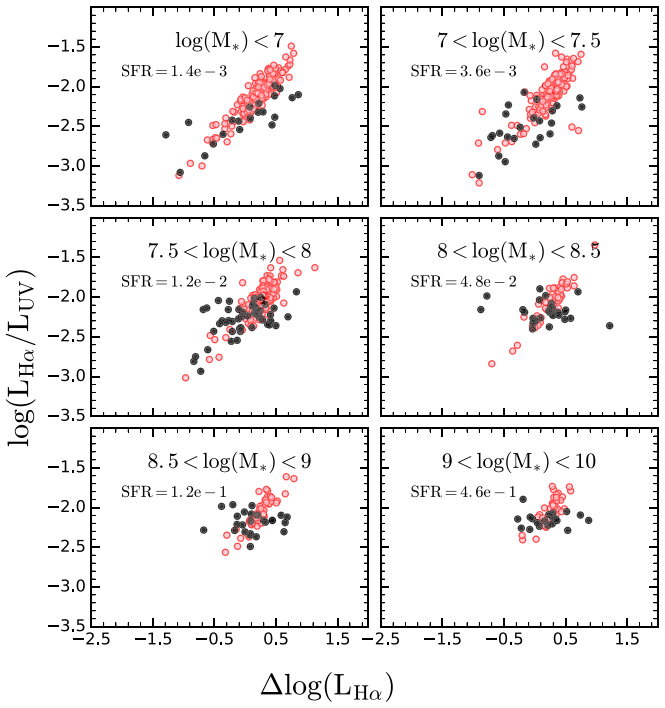


Figure 10. $\log(L_{H\alpha}/L_{UV})$ vs. $\Delta\log(L_{H\alpha})$ due to stochastic sampling of the ICMF and ISMF. Red points are SLUG-synthesized galaxies and black points are the W12 observed galaxies. The input (constant) SFR is derived from the average $L_{H\alpha}$ of the W12 sample for each mass bin. Though the SFR is constant, the luminosities change considerably as high-mass stars are stochastically created. When high-mass stars are abundant, the galaxy is high in both $\log(L_{H\alpha}/L_{UV})$ and $\Delta\log(L_{H\alpha})$. When high-mass stars are not abundant, the galaxy is low in both $\log(L_{H\alpha}/L_{UV})$ and $\Delta\log(L_{H\alpha})$. Thus, there is a tight correlation between $\log(L_{H\alpha}/L_{UV})$ and $\Delta\log(L_{H\alpha})$, with a slope of ∼1 in all mass bins.

not abundant, the galaxy is low in both $\log(L_{H\alpha}/L_{UV})$ and $\Delta\log(L_{H\alpha})$. Thus, there is a tight correlation between $\log(L_{H\alpha}/L_{UV})$ and $\Delta\log(L_{H\alpha})$, with a slope of ∼1 in all mass bins. We note that a slope of ∼1 suggests that $L_{H\alpha}$ is changing significantly, while L_{UV} is roughly constant.

The SLUG points roughly produce the width of the observed $\Delta\log(L_{H\alpha})$ distribution. However, SLUG significantly overpredicts the observed slope of the $\log(L_{H\alpha}/L_{UV})$ versus $\Delta\log(L_{H\alpha})$ trend (slope of 1 versus ∼0.5). Therefore, it appears that bursty star formation is responsible for most of the observed spread in the $\log(L_{H\alpha}/L_{UV})$ and $\Delta\log(L_{H\alpha})$ distributions. This is somewhat surprising, because the very low SFRs in our low-mass bins should suggest incomplete sampling of the high-mass end of the ISMF. This may be reconciled if star-forming clusters in gas-rich, low-mass galaxies are "top-heavy" relative to the ICMF assumed above.

Eldridge (2012) added the effect of binary stars to the stochastic IMF sampling and looked at the $\log(L_{H\alpha}/L_{UV})$ distribution of the W12 sample. Binary star mergers and mass transfer both produce more massive stars than were present in the initial population, which blurs some of the observational differences between different IMF samplings in their models. However, they conclude that the scatter in the $\log(L_{H\alpha}/L_{UV})$ distribution is not due to the IMF sampling method but depends more on the bursty SFH of each individual galaxy.

Furthermore, more constraints can be imposed on IMF sampling by limiting the ISMF and ICMF at the high-mass end, such that the maximum stellar mass in star clusters is limited by the mass of the cluster and that the mass of the cluster itself is constrained by the SFR. This method is referred to as the integrated galactic IMF (IGIMF, Kroupa & Weidner 2003). Pflamm-Altenburg et al. (2007, 2009) and Lee et al. (2009) argue that the IGIMF explains the observed $\log(L_{H\alpha}/L_{UV})$ distribution of their sample. However, Fumagalli et al. (2011) suggest that the imposed high-mass limits of both the ICMF and the ISMF in the IGIMF models lead to a dramatic reduction in the luminosity scatter at low SFRs, which is inconsistent with observations (Andrews et al. 2013, 2014).

5.3. Escape of Ionizing Photons

We note that our models consistently extend to higher $\log(L_{H\alpha}/L_{UV})$ values than are observed at all stellar masses (see Figure 6), but especially at $\log(M_*) < 8$. This ratio is affected by stellar metallicity, so part of this discrepancy could be alleviated if we assumed higher metallicity values. However, we are using metallicities that are consistent with measured mass–metallicity trends in low-redshift galaxies (Andrews & Martini 2013), and in any case the offset between the observed galaxies and models in the low-mass galaxies (∼0.3 dex) is larger than can be explained by stellar metallicity alone (∼0.1 dex difference between 0.2 $Z_\odot$ and $Z_\odot$, Bruzual & Charlot 2003). One possible explanation is that a significant fraction of the ionizing photons (roughly half) are escaping from low-mass galaxies at the peak of their burst phase, resulting in lower observed $L_{H\alpha}$. Such a high escape fraction has only been observed in a handful of galaxies with extreme star formation surface densities and sSFRs (Vanzella et al. 2016, 2018; Izotov et al. 2018), unlike the more typical galaxies in our sample. However, we note that the escape fraction has not been probed in galaxies with such low star formation rates ($SFR < 0.1\ M_\odot\ yr^{-1}$), because the Lyman continuum flux would be difficult to detect with current instrumentation. There has been an indirect search for escaping ionizing photons (via a deep search for faint Hα recombination in the nearby circumgalactic medium of three nearby dwarf galaxies. But there was only 5% more $L_{H\alpha}$ emission identified (Lee et al. 2016). This still leaves open the possibility that the ionizing photons may escape to a much larger radius (>2 kpc). The possibility that typical low-mass galaxies have high escape fractions of ionizing photons is intriguing and has important implications for reionization and the subsequent evolution of the ionizing background.

Another possible explanation is that the high-mass end of the IMF is not being fully sampled, creating a deficit of the most massive stars and suppressing $L_{H\alpha}$. However, in Figure 10, we can see that modeling of the stochastic sampling of the IMF still produces a large number of galaxies above the observed distribution of $\log(L_{H\alpha}/L_{UV})$ at all masses. Therefore, it appears that IMF sampling cannot fully explain the discrepancy.

5.4. Dust Attenuation

We caution that the $\log(L_{H\alpha}/L_{UV})$ measurements contain potential systematic uncertainties arising from the application of a uniform dust attenuation curve. We know that even galaxies with similar masses and star formation histories show considerable scatter in their extinction curves (Meurer et al. 1999). This will increase the scatter in the $\log(L_{H\alpha}/L_{UV})$ versus $\Delta\log(L_{H\alpha})$ plane, but does not significantly affect our interpretation, because it ultimately depends on the slope of the distribution in that plane. In addition, there is some evidence that attenuation curves may change as a function of stellar mass and/or SFR (Reddy et al. 2015). If the variations in attenuation

curves are a function of stellar mass, this will not affect our results, because we have binned our data in narrow stellar mass ranges. However, if the attenuation curves change as a function of SFR, then this would change the relative attenuation of $L_{\rm UV}$ and $L_{\rm H\alpha}$ within a stellar mass bin, which could change the slope of the distribution in the $\log(L_{\rm H\alpha}/L_{\rm UV})$ versus $\Delta\log(L_{\rm H\alpha})$ plane.

6. Summary

In this paper we studied the phenomenon of bursty star formation in low-redshift dwarf galaxies and attempted to determine the parameters (amplitudes and timescales) of the bursts. The parameters can be measured by comparing SFR indicators (e.g., $L_{\rm H\alpha}$ and $L_{\rm UV}$) that are sensitive to different timescales. For our analyses, we used the data from W12, which include extinction-corrected $L_{\rm H\alpha}$ and $L_{\rm UV}$ measurements for local galaxies with a large range in stellar mass ($10^6 < M_* < 10^{10} M_\odot$).

First, we fit to the same top-hat periodic burst model of W12 to determine the period, duration, and amplitude of the bursts. We improved the analysis by (1) using more appropriate sub-solar stellar metallicities, (2) expanding the probed parameter space, and (3) using a likelihood analysis to better determine parameter uncertainties and degeneracies. We found that the results were broadly similar to those of W12, but with significantly longer durations and periods. Moreover, we found that the parameters had significant uncertainties and degeneracies, with period and duration being highly degenerate. We therefore argued that it is not sufficient to use only a single $\log(L_{\rm H\alpha}/L_{\rm UV})$ distribution to constrain a three-parameter burst model.

We showed that a galaxy's location on the star-forming main sequence is correlated with the $\log(L_{\rm H\alpha}/L_{\rm UV})$ distribution, strongly suggesting that all of the galaxies are exhibiting similar star formation histories. Thus, we argue that the $\Delta\log(L_{\rm H\alpha})$ distribution (i.e., the deviation of $\log(L_{\rm H\alpha})$ from the mean $\log(L_{\rm H\alpha})$) should be used to estimate burst parameters, in addition to the $\log(L_{\rm H\alpha}/L_{\rm UV})$ distribution. Indeed, the two parameters are correlated, and the motion of galaxies in the two-dimensional $\log(L_{\rm H\alpha}/L_{\rm UV})$–$\Delta\log(L_{\rm H\alpha})$ plane gives significant insight into the timescale for variations in the SFR.

In order to avoid highly parameterized star formation histories, we look for a model with the fewest parameters that informs us most about the physical characteristics of the bursts. So we instead compare to exponential bursts with two parameters: (1) the timescale of rising and falling of the SFR (e-folding time, τ) and the maximum amplitude of the bursts (A). We find that galaxies with stellar masses less than $10^{7.5}\,M_\odot$ undergo large and rapid changes in SFR with timescales of $\tau < 30$ Myr and maximum amplitudes of $A \sim 100$, while galaxies more massive than $10^{8.5}\,M_\odot$ experience smaller, slower changes in SFR with $\tau > 300$ Myr and $A \sim 10$.

We also calculated the $\log(L_{\rm H\alpha}/L_{\rm UV})$–$\Delta\log(L_{\rm H\alpha})$ relation for galaxies in the FIRE-2 hydrodynamical simulations and found that these galaxies exhibit changes in SF on a short timescale ($\tau < 30$ Myr) at all mass ranges. Though the amplitudes of these bursts agree well with the observed $\Delta\log(L_{\rm H\alpha})$ distributions, such short bursts are different from the long timescales of $\tau > 100$ Myr that we inferred for galaxies above $10^8\,M_\odot$. Future improvements to the simulations should look carefully at what is causing such short bursts in the more massive galaxies ($M_* \gtrsim 10^8\,M_\odot$).

Furthermore, we examined the stochastic IMF sampling models using the SLUG code (da Silva et al. 2014) and found that the simulated $\log(L_{\rm H\alpha}/L_{\rm UV})$–$\Delta\log(L_{\rm H\alpha})$ distributions were significantly steeper than the observed distributions. Therefore, stochastic sampling of the IMF may help explain some of the scatter in $\log(L_{\rm H\alpha}/L_{\rm UV})$–$\Delta\log(L_{\rm H\alpha})$, but the assumptions regarding the mass function of the clusters or stars may need to be revised.

Finally, we note that measurements of $L_{\rm UV}$ already exist for large samples of galaxies from $z \sim 1$ up to the earliest epochs ($z \sim 8$). Soon, with the advent of the *James Webb Space Telescope*, *WFIRST*, and the next generation of 30 m class ground-based telescopes, measurements of $L_{\rm H\alpha}$ will be routine, even for dwarf galaxies at high redshift. As galaxies at early epochs will have very different conditions (smaller physical sizes, higher gas fractions, more metal-poor stars), it will be necessary to use a similar analysis to determine the properties of bursty star formation at high redshift. This will in turn allow us to better interpret these observables to more accurately determine physical properties.

We thank the anonymous referee for providing useful comments that helped improve the quality of this paper. N.E. and B.S. acknowledge support from Program number 13905 provided by NASA through a grant from the Space Telescope Science Institute, which is operated by the Association of Universities for Research in Astronomy, Incorporated, under NASA contract NAS5-26555. D.R.W. is supported by an Alfred P. Sloan Fellowship and acknowledges the Alexander von Humboldt Foundation.

Appendix
Details of Determining SF Model Parameters Based on the $\log(L_{\rm H\alpha}/L_{\rm UV})$ Distribution

We first describe the method of Weisz et al. (2012, W12) of constraining burst parameters, and then explain our improvements to the method.

W12 divided their observed sample into five stellar mass bins from 10^6 to 10^{11} $M_\odot$ and assumed that all galaxies of similar stellar masses have star formation histories with the same parameters. They defined their SF models as top-hat, periodic bursts superimposed on a constant, baseline SFR and assumed stellar metallicity of $1\,Z_\odot$. They then determined the $\log(L_{\rm H\alpha}/L_{\rm UV})$ distribution from models with different burst periods (P), durations (D), and amplitudes (A) and used a Kolmogorov–Smirnov test to identify the parameters that best reproduce the observed $\log(L_{\rm H\alpha}/L_{\rm UV})$ distribution in each mass bin. W12 finely sampled the parameter space, resulting in 1466 SFH models. The main conclusion of W12 is that galaxies with the lowest stellar masses have higher-amplitude bursts ($A \sim 30\times$ the baseline rate), relatively long durations ($D \sim 30$–40 Myr), and long periods ($P = 250$ Myr). The highest mass bins are characterized by almost constant SFRs with an occasional modest burst favoring SF models with short duration ($D \sim 6$ Myr) and modest amplitudes ($A \sim 10$).

We use the same periodic, top-hat burst model as W12, with the same parameters (P, D, A). The duration is restricted to be less than the period. We note that the value of the baseline SFR is irrelevant, because the relevant factor affecting luminosity ratios is the ratio of the amplitude SFR to the baseline SFR. From observations, we have a sample of $\log(L_{\rm H\alpha}/L_{\rm UV})$ for 185 local galaxies in the mass range $5 < \log(M_*[M_\odot]) < 11$. The observed sample is classified into six mass bins.

For each individual set of model parameters, we build a sample of 10,000 $\log(L_{\rm H\alpha}/L_{\rm UV})$ values for that SFH, selected in 5 Myr time intervals. This is a way of representing an ensemble of

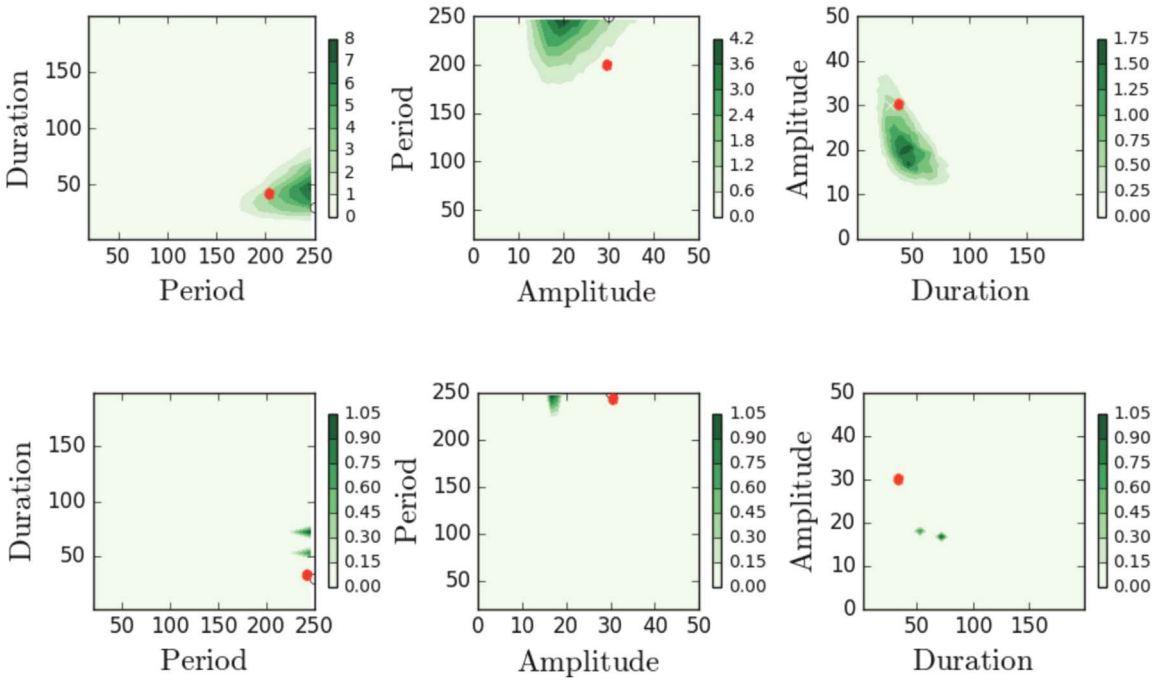


Figure 11. 2D contour plots of (D, P), (P, A) and (A, D) from left to right. Parameter space is limited to the W12 range, i.e., $D \leqslant 200$, $P \leqslant 250$, $A < 50$ and assumes a stellar metallicity of 1 $Z_{\odot}$. Top and bottom subplots are contour plots of $M \leqslant 10^7\ M_{\odot}$ and $10^7 < M \leqslant 10^8\ M_{\odot}$ respectively. The maximum likelihood values are in good agreements with the W12 predictions, shown as red circles.

galaxies in the real world that are caught during different stages of the SFH, assuming that they all share the same SFH. We do not sample the first 200 Myr of star formation, to ensure that $L_{\rm UV}$ is not biased low because it would not have enough time to build up a full sample of A-stars. To do this, we first calculate the SED as a function of time for a single stellar population (Bruzual & Charlot 2003) using a Chabrier IMF (Chabrier 2003), Padova isochrones (Bressan et al. 1993; Bertelli et al. 1994; Fagotto et al. 1994), and a constant stellar metallicity. For each output SED, we calculate $L_{\rm UV}$ as the average of the continuum between 1460 and 1540 Å and $L_{\rm H\alpha}$ by determining the hydrogen-ionizing photon production rate and assuming case-B recombination. We then convolve our $L_{\rm UV}(t)$ and $L_{\rm H\alpha}(t)$ curves with the SFR(t) curves to determine the intrinsic (unobscured by dust) $\log(L_{\rm H\alpha}/L_{\rm UV})$ as a function of time.

To take into account the observational uncertainties, we add 10%–20% Gaussian errors to $L_{\rm UV}$ and $L_{\rm H\alpha}$ due to statistical uncertainties arising from dust attenuation corrections (see Section 4.1).

Finally, we determine the probability of obtaining our measured distribution of $\log(L_{\rm H\alpha}/L_{\rm UV})$ given the modeled distribution for the set of parameters (D, P, A). We then determine the set of parameters that maximizes the probability space and marginalize them to determine the 1D posterior distributions for each individual parameter.

In order to select the appropriate metallicity for each stellar mass bin, we refer to the mass–metallicity relation from Andrews & Martini (2013), assuming the solar oxygen abundance to be 8.86. In Table 2, the approximate metallicity of each mass bin is determined except for the lowest one due to a lack of data points in this mass range. We choose to use the metallicities from the existing libraries in Bruzual & Charlot (2003) that are closest to the values in the second column of Table 2. The chosen metallicities are given in the third column. For $M \leqslant 10^7\ M_{\odot}$ we assumed 0.2 solar metallicity because the next smallest metallicity available in the BC03 is 0.02 $Z_{\odot}$, far lower than we expect for galaxies at those stellar masses. The results of this model are discussed in Section 3.

A.1. Improvements to Fits to Periodic SF History

As discussed above, the W12 study made significant progress in fitting to the $\log(L_{\rm H\alpha}/L_{\rm UV})$ distribution to determine parameters of the SF burst model. However, we have identified ways in which we can enhance the W12 analysis.

First, the stellar metallicity was assumed to be solar for all mass ranges. This can change the estimated SF model parameters because stellar metallicity affects the surface temperature of stars such that more metal-rich stars are cooler at a given mass. This therefore affects the proportion of ionizing and non-ionizing photons. To address that, we explore the effects of using more realistic (lower) stellar metallicities on parameter estimation for different mass ranges based on the metallicities estimated in Andrews & Martini (2013) (see Table 2).

Second, in order to explore the model parameter space, W12 used a two-sided Kolmogorov–Smirnov test. However, we use a likelihood approach that allows us to better determine parameter uncertainties and degeneracies.

Third, the best-fit parameters from W12 were at the edge of the explored parameter space, so it is possible that the actual best-fit parameters are out of the explored range. Therefore, we expanded the parameter space (by a factor of five in duration, period, and amplitude) in order to guarantee that we explore all the parameter space far enough to encompass the best-fit parameter.

A.2. Results of Best-fit Burst Parameters

We first test our method by comparing our analysis with that of W12 to see whether we produce the same best-fit values. To do so, we make the same assumptions as W12 (assuming solar metallicity and identical parameter space). Figure 11 shows the

contours of the burst parameters for the two lowest mass ranges in W12, i.e., $M \leqslant 10^7\ M_\odot$ and $10^7 < M \leqslant 10^8\ M_\odot$.

As can be seen in Figure 11, the best-fit parameters are in agreement with W12. They report (D, P, A) of (40, 200, 30) and (30, 250, 30) for $M \leqslant 10^7\ M_\odot$ and $10^7 < M \leqslant 10^8\ M_\odot$ respectively, which are comparable to our results: (46, 250, 20) (Figure 11, top) and (53, 250, 18) (Figure 11, bottom). The slight discrepancy in the duration and amplitude between our method and W12 arises from the different sampling of the parameter space. This confirms the credibility of our maximum likelihood approach for determining the best-fit parameters of bursts. The results and the interpretations are discussed in Section 3.

ORCID iDs

Najmeh Emami https://orcid.org/0000-0003-2047-1689
Brian Siana https://orcid.org/0000-0002-4935-9511
Daniel R. Weisz https://orcid.org/0000-0002-6442-6030
Benjamin D. Johnson https://orcid.org/0000-0002-9280-7594
Xiangcheng Ma https://orcid.org/0000-0001-8091-2349
Kareem El-Badry https://orcid.org/0000-0002-6871-1752

References

Andrews, B. H., & Martini, P. 2013, ApJ, 765, 140
Andrews, J. E., Calzetti, D., Chandar, R., et al. 2013, ApJ, 767, 51
Andrews, J. E., Calzetti, D., Chandar, R., et al. 2014, ApJ, 793, 4
Bertelli, G., Bressan, A., Chiosi, C., Fagotto, F., & Nasi, E. 1994, A&AS, 106, 275
Bicker, J., & Fritze-v. Alvensleben, U. 2005, A&A, 443, L19
Boselli, A., Boissier, S., Cortese, L., et al. 2009, ApJ, 706, 1527
Bouwens, R. J., Illingworth, G. D., Oesch, P. A., et al. 2015, ApJ, 811, 140
Bressan, A., Fagotto, F., Bertelli, G., & Chiosi, C. 1993, A&AS, 100, 647
Bruzual, G., & Charlot, S. 2003, MNRAS, 344, 1000
Chabrier, G. 2003, PASP, 115, 763
Choi, J., Conroy, C., & Byler, N. 2017, ApJ, 838, 159
da Silva, R. L., Fumagalli, M., & Krumholz, M. 2012, ApJ, 745, 145
da Silva, R. L., Fumagalli, M., & Krumholz, M. R. 2014, MNRAS, 444, 3275
de Jong, R. S., & Lacey, C. 2000, ApJ, 545, 781
Domínguez, A., Siana, B., Brooks, A. M., et al. 2015, MNRAS, 451, 839
Duncan, K., & Conselice, C. J. 2015, MNRAS, 451, 2030
El-Badry, K., Quataert, E., Wetzel, A., et al. 2018, MNRAS, 473, 1930
Eldridge, J. J. 2012, MNRAS, 422, 794
Fagotto, F., Bressan, A., Bertelli, G., & Chiosi, C. 1994, A&AS, 105, 29
Fall, S. M., Chandar, R., & Whitmore, B. C. 2009, ApJ, 704, 453
Fitts, A., Boylan-Kolchin, M., Bullock, J. S., et al. 2018, MNRAS, 479, 319
Fumagalli, M., da Silva, R. L., & Krumholz, M. R. 2011, ApJL, 741, L26
Glazebrook, K., Blake, C., Economou, F., Lilly, S., & Colless, M. 1999, MNRAS, 306, 843
Governato, F., Brook, C., Mayer, L., et al. 2010, Natur, 463, 203
Guo, Y., Rafelski, M., Faber, S. M., et al. 2016, ApJ, 833, 37
Hopkins, P. F., Kereš, D., Oñorbe, J., et al. 2014, MNRAS, 445, 581
Hopkins, P. F., Wetzel, A., Kereš, D., et al. 2018, MNRAS, 480, 800
Hoversten, E. A., & Glazebrook, K. 2008, ApJ, 675, 163
Iglesias-Páramo, J., Boselli, A., Gavazzi, G., & Zaccardo, A. 2004, A&A, 421, 887
Izotov, Y. I., Worseck, G., Schaerer, D., et al. 2018, MNRAS, 478, 4851
Kauffmann, G. 2014, MNRAS, 441, 2717
Kennicutt, R. C., & Evans, N. J. 2012, ARA&A, 50, 531
Kennicutt, R. C., Jr. 1998, ARA&A, 36, 189
Kennicutt, R. C., Jr., Lee, J. C., Funes, J. G., et al. 2008, ApJS, 178, 247
Kereš, D., Katz, N., Davé, R., Fardal, M., & Weinberg, D. H. 2009, MNRAS, 396, 2332
Kewley, L. J., Geller, M. J., Jansen, R. A., & Dopita, M. A. 2002, AJ, 124, 3135
Kroupa, P., & Weidner, C. 2003, ApJ, 598, 1076
Lada, C. J., & Lada, E. A. 2003, ARA&A, 41, 57
Lee, J. C., de Paz, A. G., Jr, Kennicutt, R. C., et al. 2011, ApJS, 192, 6
Lee, J. C., Gil de Paz, A., Tremonti, C., et al. 2009, ApJ, 706, 599
Lee, J. C., Veilleux, S., McDonald, M., & Hilbert, B. 2016, ApJ, 817, 177
Mehta, V., Scarlata, C., Rafelski, M., et al. 2017, ApJ, 838, 29
Meurer, G. R., Heckman, T. M., & Calzetti, D. 1999, ApJ, 521, 64
Meurer, G. R., Wong, O. I., Kim, J. H., et al. 2009, ApJ, 695, 765
Pflamm-Altenburg, J., Weidner, C., & Kroupa, P. 2007, ApJ, 671, 1550
Pflamm-Altenburg, J., Weidner, C., & Kroupa, P. 2009, MNRAS, 395, 394
Reddy, N. A., Kriek, M., Shapley, A. E., et al. 2015, ApJ, 806, 259
Robertson, B. E., Furlanetto, S. R., Schneider, E., et al. 2013, ApJ, 768, 71
Shapley, A. E., Steidel, C. C., Pettini, M., Adelberger, K. L., & Erb, D. K. 2006, ApJ, 651, 688
Siana, B., Teplitz, H. I., Colbert, J., et al. 2007, ApJ, 668, 62
Somerville, R. S., & Primack, J. R. 1999, MNRAS, 310, 1087
Sparre, M., Hayward, C. C., Feldmann, R., et al. 2017, MNRAS, 466, 88
Springel, V., Di Matteo, T., & Hernquist, L. 2005, MNRAS, 361, 776
Steidel, C. C., Pettini, M., & Adelberger, K. L. 2001, ApJ, 546, 665
Vanzella, E., de Barros, S., Vasei, K., et al. 2016, ApJ, 825, 41
Vanzella, E., Nonino, M., Cupani, G., et al. 2018, MNRAS, 476, L15
Weisz, D. R., Johnson, B. D., Johnson, L. C., et al. 2012, ApJ, 744, 44
Zhang, Q., & Fall, S. M. 1999, ApJL, 527, L81